Outdoor to Indoor Propagation Channel Measurements at 28 GHz

C. Umit Bas, *Student Member, IEEE*, Rui Wang, *Student Member, IEEE*, Seun Sangodoyin, *Student Member, IEEE*, Thomas Choi, *Student Member, IEEE*, Sooyoung Hur, *Member, IEEE*, Kuyeon Whang, *Member, IEEE*, Jeongho Park, *Member, IEEE*, Jianzhong Zhang, *Fellow, IEEE*, Andreas F. Molisch, *Fellow, IEEE*

***Abstract*—Outdoor to indoor penetration loss is one of the crucial challenges faced at millimeter-wave frequencies. This paper presents the results from 28 GHz channel sounding campaigns performed to investigate the impact of this phenomenon on the wireless propagation channel characteristics in small cell and fixed wireless access scenarios. The measurements are performed with a real-time channel sounder equipped with phased array antennas that allow beam-forming and electronic beam steering for directionally resolved measurements. Thanks to the short measurement time and the excellent phase stability of the system, we obtain both directional and omnidirectional channel power delay profiles without any delay uncertainty. We compare the measured path loss, delay spread and angular spread for indoor and outdoor receiver locations for two different types of buildings. We find that the penetration loss strongly depends on the angle of incidence, and that the scatterers on the outside of the building strongly impact how much power is coupled into the building. Based on the results, we provide statistical models for path loss, delay spread, and angular spread.**

I. Introduction

The number of connected devices and their data requirements have been increasing exponentially. Especially with the introduction of new applications such as augmented reality, virtual reality, and Ultra-HD video streaming, monthly global IP traffic is expected to reach 278 exabytes by 2021 [2]. While a variety of different techniques will be employed in 5G to enable this growth [3], [4], utilizing the fallow spectrum beyond 6 GHz is among the most promising approaches [5]. Gbps broadband connections to multiple users can be realized by exploiting the large bandwidths available at mm-wave frequencies [6], [7].

An accurate channel model is crucial for any efficient wireless system design. The prospect of mm-wave wireless systems has thus fueled interest in mm-wave propagation channel measurements, e.g., [8], [9]. Since many of the future applications will demand connectivity between outdoor base stations and indoor users, outdoor to indoor (O2I) penetration is one of the most important factors affecting the performance of mm-wave systems. Not only does the penetration loss take on higher values than at cm-wave frequencies, but it also is highly sensitive to the several factors such as density or the construction material types. Furthermore, at mm-wave frequencies, the angular characteristics of the propagation channel are of the utmost importance, since these systems are highly dependent on the beam-forming gain to overcome the higher path loss occurring at higher frequencies [10].

C. U. Bas, R. Wang, T. Choi, S. Sangodoyin and A.F. Molisch are with the Department of Electrical Engineering, University of Southern California (USC), Los Angeles, CA 90089-2560 USA. J. Zhang is with Samsung Research America, Richardson, TX, USA. S. Hur, K. Whang and J. Park are with Samsung Electronics, Suwon, Korea.

An earlier version of this work appeared in the Proceedings of IEEE International Conference on Communications 2018 [1].

Part of this work was supported by the National Science Foundation under projects ECCS-1126732 and CIF-1618078 and by the National Institute of Standards and Technology under grant 60NANB17D317.

A. Existing Literature

Most of the current literature at $28\,\mathrm{GHz}$ focuses on outdoor to outdoor (O2O) or indoor to indoor (I2I) measurements, e.g., [11]–[16] and references therein. As an exception from this trend, [17] reported O2I measurements at $28\,\mathrm{GHz}$ by using a rotating horn antenna channel sounder which can provide an accurate absolute delay as well as angular information. The paper observed a larger number of clusters, larger excess delays and larger angular spreads indoor compared to the corresponding outdoor locations. However, there was a limited number of indoor receiver (RX) locations and a single type of building was investigated. Ref. [18] performed narrowband measurements at $28\,\mathrm{GHz}$ where the RX was in an office building, and reported O2I penetration loss values varying from $3\,\mathrm{dB}$ to $60\,\mathrm{dB}$ depending on the RX location and the construction material types. However, the measurements were performed for highly directional receivers and do not consider the effects of scattering-rich indoor environments on the angular spectrum. Furthermore due to the limited bandwidth, the delay spread statistics were not considered. Similarly, [19] presents narrowband building penetration measurements in a suburban residential neighborhood. It proposes a *common-slope cross-comparison method* and estimates building penetration losses varying from 9 dB to 17 dB. Ref. [20] investigates the penetration loss for external and internal walls at different carrier frequencies ranging from $0.8\,\mathrm{GHz}$ to $28\,\mathrm{GHz}$ with narrowband signals, and proposes a linear model for frequency dependency of the penetration loss. In [21], the authors present results for penetration loss and reflection coefficient measurements for different types of building materials. For example; the penetration loss for clear glass is measured as $3.9\,\mathrm{dB}$ while it is $40\,\mathrm{dB}$ for tinted glass. However, the reported O2I measurement are resembling a device-to-device use case rather than a cellular deployment. A summary of penetration loss results, and a frequency-dependent model, is given in [22] and also used in 3GPP. None of references [18]–[22] provide any delay or angular statistics.

There are other studies investigating the O2I propagation channel at different mm-wave frequencies. Ref. [23] provides delay and angular statistics at 20 GHz for one office building on different floors. For an urban micro-cellular environment, [24] presents the penetration loss at 26 GHz and 37 GHz, and compares it with microwave frequencies. It also reports the effect of incident angle on penetration loss and compares the measurement results with the 3GPP and IMT-Advanced models, however, it does not discuss delay spread or angular spread. [25] investigates the O2I penetration loss and delay spreads for the O2I channels at 60 GHz with a 10 m distance from the base-station to the building under test. Hence, both the frequency and the measurement scenario are different than this paper.

B. Our Contribution

In this work, we present the results from 28 GHz channel sounding campaigns performed to investigate the effects of O2I penetration on the wireless propagation channel characteristics. The measurement scenarios were designed to imitate a challenging propagation scenario where the direct path arrives to the front facade of the target building with a quasi-grazing angle. A real-time channel sounder equipped with phased array antennas was used for the measurements [26], [27]. The phased arrays form beams at the transmitter (TX) and RX and switch between these beams in microseconds, enabling directionally resolved results while ensuring minimal variation in the environment during the measurements. Furthermore, with the help of beam-forming gain, the channel sounder provides a measurable path loss of 169 dB. We compare the O2O and O2I channel characteristics and report the effects of O2I penetration on the received power, the angular spread of the direction of arrival (DoA) and the delay spread. Furthermore, we compare these channel characteristics for omnidirectional and directional RX cases. Finally, we investigate the available beam diversity and the expected additional loss due to a blocked sector.

C. Paper Organization

The rest of the paper is organized as follows. Section II describes the measurement equipment and the details about the measurement scenarios under investigation. Section III presents the results and compares the propagation parameters for O2O and O2I channels. Finally, Section IV summarizes results and presents conclusions for system design.

II. Measurement Campaign

A. Measurement Environments

The measurements were performed at three different locations on or near the University of Southern California campus. For all cases, the RX was on the first floor, while the TX was on a scissor lift at the height of 5 m imitating an urban small cell scenario. To investigate the more challenging cases, we chose buildings surrounded by foliage and made sure the angle of the direct path is quasi-grazing with respect to the front facade of the target building.

Fig. 1. TX and RX locations for SFU1

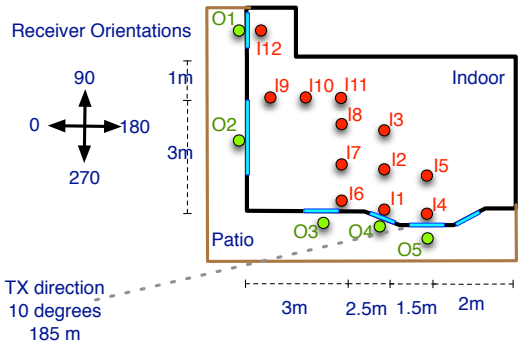

Fig. 2. Layout of RX points for SFU1, the important lengths are given in the figure in meters and sketches might not be up-to-scale.

Fig. 3. TX and RX locations for SFU2

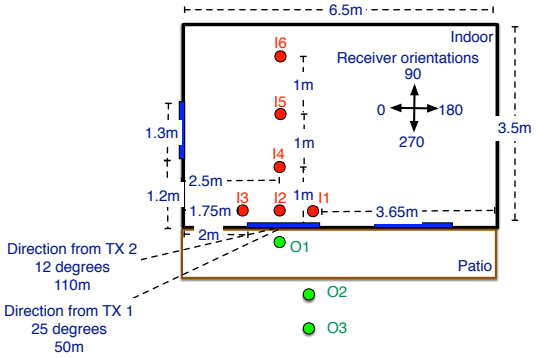

Fig. 4. Layout of RX points for SFU2, the important lengths are given in the figure in meters and sketches might not be up-to-scale.

1) Single-Family Units: We performed O2I measurements in two different single-family units (SFU). Fig. 1 shows TX and RX locations on the campus for the first SFU which is named SFU1. The building is a two-story, detached, single-family unit built using wood frames and drywalls, as is typical in California. There is also a covered, first-floor patio wrapping around the building. Measurement points are marked in Fig. 2. There are 5 outdoor points placed right in front of the windows on the patio. 12 indoor measurement locations are placed throughout the room as the furniture allows. All RX points

Fig. 5. TX and RX locations for BOB

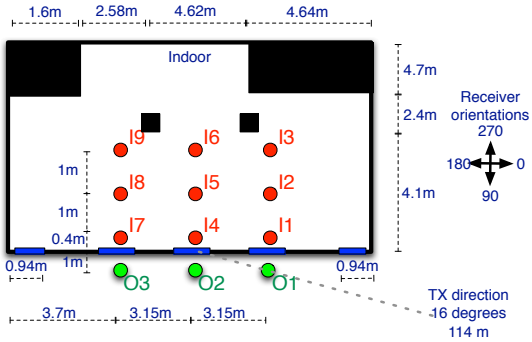

Fig. 6. Layout of RX points for the BOB, the important lengths are given in the figure in meters and sketches might not be up-to-scale.

are at 1.8 m height above the first floor. The TX is placed on the same street as the house at a distance of $185\,\mathrm{m}$ at an angle of 10° according to the given directions in Fig. 1. The direct path from the TX to the house is blocked by foliage from trees. Additionally, points *O1* and *O2* are also shadowed by the building across the street.

The second SFU (SFU2) has a similar structure as SFU1 except the fact that SFU1 was on the corner of an intersection while SFU2 is not, as seen in Fig. 3. In this case, we repeated the measurements for two TX points; TX1 and TX2. TX1 is located 50 m away from the house and at the angle of 25°, Fig. 4. TX2 is a more challenging location as it is placed 110 m away from the house at the angle of 12°. Furthermore, the side window (the window facing 0°) is visible from TX1, while it is blocked by the neighboring house in case of TX2. For both TX locations, the TX height is 5 m. The RX heights for all indoor points and *O1* are 1.8 m above the first floor while the points *O2* and *O3* are 1.8 m with respect to the street level.

2) Brick Office Building: The second measurement scenario is a multi-story, brick building (BOB) surrounded by heavy foliage as shown in Fig. 5. The TX-RX distance is $114\,\mathrm{m}$, and the angle of the direct path is 16°. Three outdoor measurement locations are just outside of the three front-facing windows. For each window, there are three indoor locations placed on a line along with the corresponding outdoor point. The distances of the indoor measurement points from the window are $0.4\,\mathrm{m}$, $1.4\,\mathrm{m}$ and $2.4\,\mathrm{m}$, see Fig. 6.

The outdoor RX points are distributed in front of the buildings facades facing towards the TX. Spefically, the outdoor RX points are chosen in front of the windows, since most of the received power arrives through windows (see Section III-A). This placement also allows a one-to-one comparison of the multi-path-components (MPCs) observed by the indoor and outdoor RXs. Hence, it provides insights into the effects of O2I propagation on different types of paths from TX to RX. In case of SFU2, the limited area in front of the window could accommodate only one RX point (*O1*), the received power for two other locations (*O2 and O3*) away from the windows are also provided for readers' references. We finally notice that none of the windows is of the energy-saving type. This has important consequences for propagation, since energy-saving windows. which are typically covered with a thin metal film, have much higher attenuation than regular ones.

TABLE I
SOUNDER SPECIFICATIONS

Hardware Specifications	
Center frequency	27.85 GHz
Instantaneous bandwidth	400 MHz
Antenna array size	8 by 2
Horizontal beam steering (RX/TX)	360° / 90°
Horizontal 3dB beam width	12°
Vertical beam steering (RX/TX)	-30° to 30° / 0°
Vertical 3dB beam width	22°
Horizontal/Vertical steering steps	5° / 10°
Beam switching speed	$2\mu s$
TX EIRP	57 dBm
RX noise figure	$\leq$ 5 dB
ADC/AWG resolution	10/15-bit
Data streaming speed	700 MBps
Sounding Waveform Specifications	
Waveform duration	2 μs
Repetition per beam pair	10
Number of tones	801
Tone spacing	500 kHz
PAPR	0.4 dB
Total sweep time	101.08 ms (each 90° sector)

B. Measurement Setup

In this campaign, we used a switched-beam, real-time, wide-band mm-wave sounder with 400 MHz bandwidth [26], [27]. The sounding signal is a multi-tone signal which consists of equally spaced 801 tones covering 400 MHz. A low peak to average power ratio (PAPR) of 0.4 dB is achieved by adjusting the phases of individual tones as suggested in [28]. This allows to transmit with power as close as possible to the 1 dB compression point of the power amplifiers without driving them into saturation.

Both the TX and the RX are equipped with 2 by 8 rectangular phased array antennas capable of forming beams that can be electronically steered with 5° resolution in the range of $[-45^\circ, 45^\circ]$ in azimuth and $[-30^\circ, 30^\circ]$ in elevation. During this measurement campaign we utilize a single elevation angle, 0°, with 19 azimuth angles for the TX, and 7 elevation angles along with 19 azimuth angles for the RX. With an averaging factor of 10, the total sweep time is $101.08\,\mathrm{ms}$ for 2527 total beam pairs. Since phased arrays cover 90° sectors, we rotated the RX to $\{0^\circ, 90^\circ, 180^\circ, 270^\circ\}$ to cover 360° while using a single orientation at the TX. Consequently, for each

measurement location, we obtain a frequency response matrix of size 7 by 72 by 19 by 801.

Moreover, thanks to the beam-forming gain, the TX equivalent isotropically radiated power (EIRP) is $57\,\mathrm{dBm}$, and the measurable path loss is $159\,\mathrm{dB}$ without considering any averaging or spreading gain. Including the averaging ratio used in this campaign, the measurable path loss is $169\,\mathrm{dB}$. By using GPS-disciplined Rubidium frequency references, we were able to achieve both short-time and long-time phase stability. Combined with the short measurement time this limits the phase drift between TX and RX, enabling phase-coherent sounding of all beam pairs even when TX and RX are physically separated and have no cabled connection for synchronization.

Consequently, the directional power delay profiles (PDP) can be combined easily to acquire the omnidirectional PDP. Table I summarizes the detailed specification of the sounder and the sounding waveform. References [26] and [27] discuss further details of the sounder setup, the validation measurements, and the data processing.

C. Data Processing

In the following, we describe the post processing of the measured data using Fourier-resolution techniques. The directional power delay profile (PADP) for the TX and RX beams with the azimuth angles ϕ_{TX}, ϕ_{RX}, respectively and RX elevation angle θ_{RX} is estimated as

$$PADP(\phi_{\mathrm{TX}},\theta_{\mathrm{RX}},\phi_{\mathrm{RX}},\tau)=\left|\mathcal{F}^{-1}\left\{W\left(\vec{f}\right)\cdot H_{\phi_{\mathrm{TX}},\theta_{\mathrm{RX}},\phi_{\mathrm{RX}}}\left(\vec{f}\right)./H_{\mathrm{cal}}\left(\vec{f}\right)\right\}\right|^2 \tag{1}$$

where $\phi_{\mathrm{RX}}\in[-180,175]$, $\phi_{\mathrm{TX}}\in[-45,45]$, $\theta_{\mathrm{RX}}\in[-30,30]$, $\mathcal{F}^{-1}$ denotes inverse Fourier transform, $H_{\phi_{\mathrm{TX}},\theta_{\mathrm{RX}},\phi_{\mathrm{RX}}}$ is the frequency response for the TX beam direction ϕ_{TX} and the RX beam direction $(\theta_{\mathrm{RX}},\phi_{\mathrm{RX}})$ and $H_{\mathrm{cal}}(\vec{f})$ is the calibration response; $W(\vec{f})$ is the normalized Hanning Window, $\vec{f}$ is the vector of frequency tones, and $./$ is element-wise division. Since all beam pairs are measured without a significant phase drift or trigger jitter, all directional PDPs are already aligned in the delay domain and require no further correction. To extract MPCs, we perform peak detection in 4-D space in $PADP(\phi_{\mathrm{TX}},\theta_{\mathrm{RX}},\phi_{\mathrm{RX}},\tau)$. Then, for each delay bin we filter the ghost MPCs caused by side-lobes in the beam pattern as follows: The strongest peak detected at each delay is accepted as MPC since it can not be due to a side-lobe. Any other peaks with the same delay and within 10 dB of the strongest MPC in the same delay bin are also accepted as valid MPCs, since the sidelobes are always less than -10 dB with respect to the main lobe. Furthermore, the peaks with powers within 20 dB of the strongest MPC and where both direction of departure and the direction of arrival are different than the strongest MPC in the same delay bin are also accepted as valid MPCs. Further details of the MPC extraction are described in [27].

After the MPC extraction, the extracted MPCs are used to calculate the path loss, delay spread and angular spread statistics. The resulting delay resolution is $2.5\,\mathrm{ns}$ and the angular resolutions are 5° and 10° for azimuth and elevation, respectively. The 5° increment in the beam direction is identical to the achievable resolution of the sounder in the angular domain The RX elevation resolution of 10° is not sufficient to study angular statistics in elevation. However, the elevation steering ensures estimating true power reflected from nearby objects at different heights including the window frames and furniture. Further details of the post-processing are described in [26], [27]. To reduce the effects of noise, we remove the MPCs whose power are below the noise threshold which is set to be 6 dB above the noise floor. The noise floor is computed from the noise-only region of the PADP (samples before the first MPC). The root mean square delay spread (RMS-DS) τ_{RMS} is computed as the second central moment of the PDP [29].

$$\tau_{\mathrm{RMS}}=\sqrt{\frac{\sum_{k=1}^{N_p}\left(\tau_k-\bar{\tau}\right)^2 P_k}{\sum_{k=1}^{N_p}P_k}} \tag{2}$$

where N_p is the number of MPCs, τ_k and P_k are delay and power of k'th MPC and $\bar{\tau}$ is the mean delay, which is given by

$$\bar{\tau}=\sqrt{\frac{\sum_{k=1}^{N_p}\tau_k P_k}{\sum_{k=1}^{N_p}P_k}}. \tag{3}$$

The angular spread S_ϕ for RX azimuth is calculated as follows [30].

$$S_\phi=\sqrt{\frac{\sum\limits_{\phi}|exp(j\phi)-\mu_\phi|^2 APS(\phi)}{\sum\limits_{\phi}APS(\phi)}} \tag{4}$$

and

$$\mu_\phi=\frac{\sum\limits_{\phi}exp(j\phi)APS(\phi)}{\sum\limits_{\phi}APS(\phi)} \tag{5}$$

where $\phi\in[-\pi,\pi)$, $APS(\phi)$ is the angular power spectrum. Furthermore the mean angle is given by the angle of μ_ϕ.

III. Results

A. Multi-path Components

In this section, we discuss deterministic results to understand the effects of different scenarios on the propagation channel. We study the distribution of the extracted MPCs and compare them with the photos taken from the RX point of view[1] and the floor plans.

First, we compare the indoor and outdoor locations for the BOB. Fig. 7 shows the MPCs observed outside at *BOB-O1*. Fig. 9 shows the PADP for the same location. The strongest MPC is at 15° and it is the *line-of-sight* (LOS) path propagating through the foliage with smallest delay. Additionally, the second cluster of MPCs with $\phi_{\mathrm{RX}}\in[-50^\circ,-5^\circ]$ and slightly more delay compared to the first path are due to reflections from the building under investigation. The MPCs that have $\phi_{\mathrm{RX}}\in[20^\circ,180^\circ]$ are caused by reflections some further-away objects (e.g., buildings and poles), they have larger delays and less path gain due to the larger propagation distance.

[1]Due to height difference between camera and actual antenna, and the fish-eye lens effect the observed elevation angles in the photos are distorted.

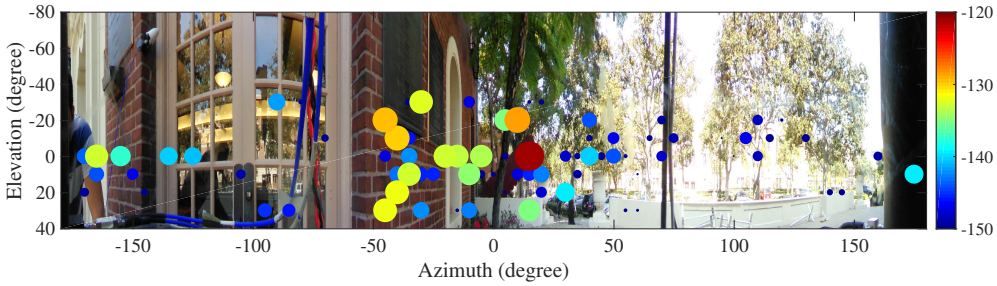

Fig. 7. Detected MPCs vs DoA - outdoor *BOB-O1*, the color and the size of the point indicate the path gain of the MPC

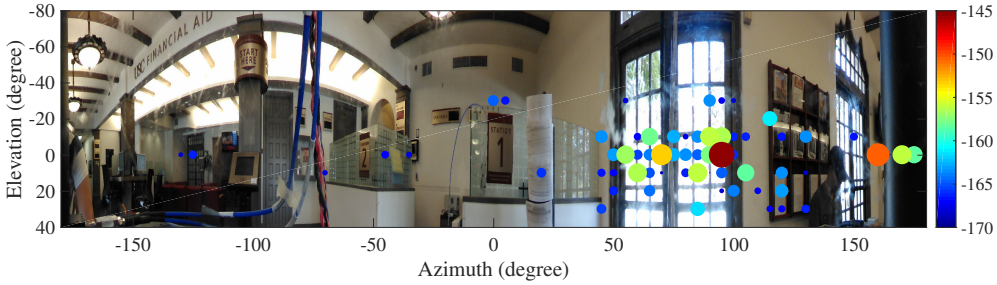

Fig. 8. Detected MPCs vs DoA - indoor *BOB-I2*, the color and the size of the point indicate the path gain of the MPC

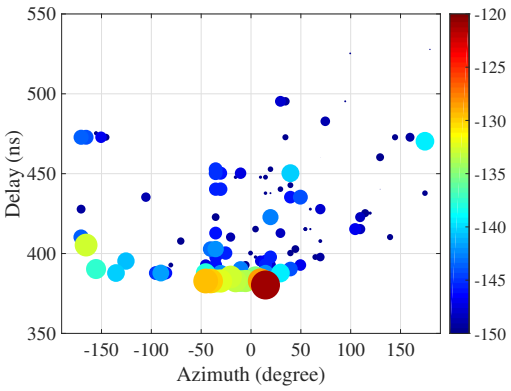

Fig. 9. MPCs vs delay and DoA - outdoor *BOB-O1*, the color and the size of the point indicate the path gain of the MPC

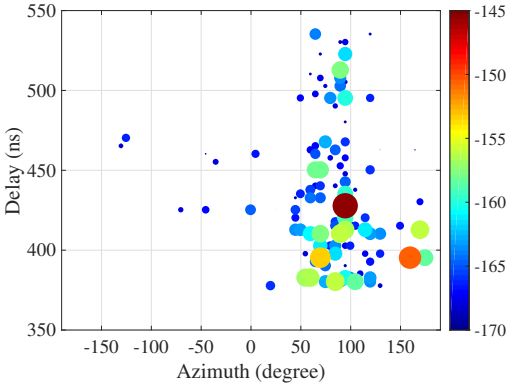

Fig. 10. MPCs vs delay and DoA - indoor *BOB-I2*, the color and the size of the point indicate the path gain of the MPC

For the indoor location in Fig. 8, we see that almost all of the MPCs are entering the building via the windows, as the brick walls do not allow any significant penetration. Fig. 10 shows the PADP for the same environment. The MPCs with the smallest delay also have the same DoA of $15°$ as the direct path outdoors, indicating that this is the path through the brick wall. However, this path is attenuated by more than 45 dB. After the first MPCs, there is the first cluster of MPCs with delays less than $400\,\mathrm{ns}$, which are caused by the interactions of the direct path with the window frames. When we compare the path gains of these MPCs with the direct path observed outdoor, we see that the excess loss is more than 30 dB, caused by the large incident angle. However, the other MPCs, which are reflected by surrounding structures, have more favourable angles of incidence. Consequently, their path gain only decreases by 5 dB to 15 dB compared to the outside locations. This indicates the effects of O2I penetration loss does not only depend on the structure under investigation but it also depends on the surrounding structures. Furthermore, this weighting of MPCs increases the indoor RMS-DS. The effects of these phenomena on the O2I penetration loss, RMS-DS and angular spread will be further discussed in Sections III-C and III-D.

Figs. 11 and 13 show the DoAs and the PADP for the outdoor location *SFU1-O3*, respectively. For this location, there is a dominant first cluster that consists of the direct path ($\phi = 10°$) and some additional paths ($\phi \in [-50°, 50°]$) due to the interaction of the direct path with the building under investigation. In addition, there are reflections from the surrounding structures with relatively larger delay. Next, we compare the MPCs observed outdoor with an indoor location *SFU1-I7* as shown in Figs. 12 and 14. SFU1 is a corner house with large windows on two sides, which are both illuminated by the TX (compare Fig. 2). In addition to the MPCs through

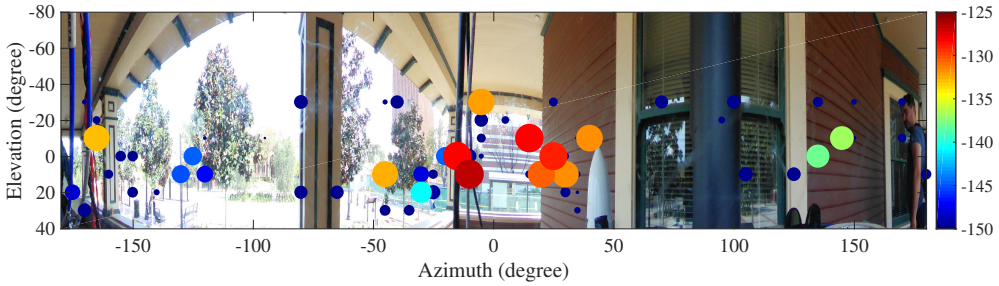

Fig. 11. Detected MPCs vs DoA - outdoor *SFU1-O3*, the color and the size of the point indicate the path gain of the MPC

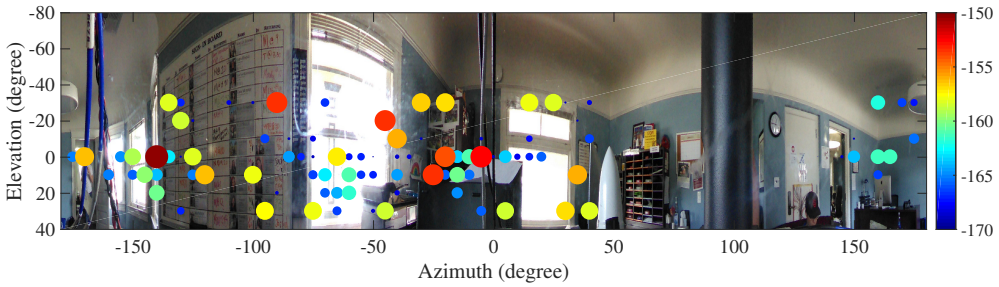

Fig. 12. Detected MPCs vs DoA - indoor *SFU1-I7*, the color and the size of the point indicate the path gain of the MPC

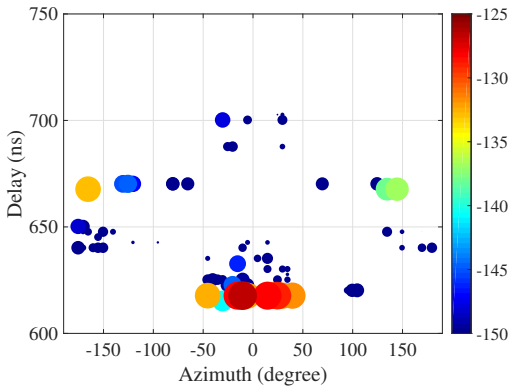

Fig. 13. MPCs vs delay and DoA - outdoor *SFU1-O3*, the color and the size of the point indicate the path gain of the MPC

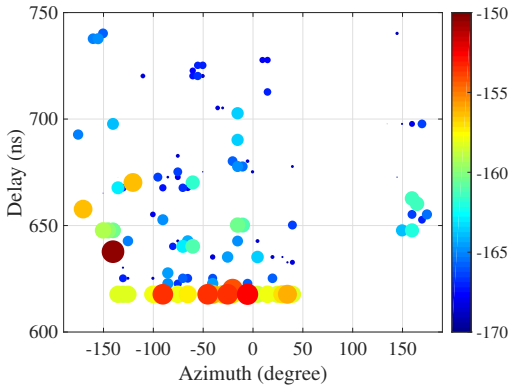

Fig. 14. MPCs vs delay and DoA - indoor *SFU1-I7*, the color and the size of the point indicate the path gain of the MPC

windows, there are several additional MPCs entering the house through the walls, which were built by wooden frames and drywalls. The MPCs with a DoA between $-50°$ and $0°$ have similar delays to the first paths observed at the outdoor location. This indicates that these MPCs arrive to the RX after penetrating the wall as seen in Fig. 12. Additionally, there are other MPCs that are reflected by the window frames or the back wall. Consequently, we see a larger range of azimuth angles indoors, compared to the BOB.

Figs. 15, 16 and 17 visualize the direction of the dominant paths for all RX locations. Due to demonstration purposes for each location only the strongest 5 paths are shown along with the mean angle or arrival.[2] As seen in Fig. 15, for every RX point, the observed set of paths varies depending on the exact location within the house. As a result of this, the angular spread values and the mean angles change significantly depending on the RX location within the room.

Although SFU2's building materials are similar to those of SFU1, as seen in Fig. 16, the observed MPCs are mostly arriving from the front side of the building since the neighboring structures block the side wall. Hence, most of the dominant paths enter the buildings via the front side. The resulting angular distribution of the MPCs in SFU2 is thus more similar to that of the BOB shown in Fig. 17. Furthermore, the mean angles for indoor RX locations are always towards the windows.

In summary, in a realistic environment, there will be multiple paths arriving from the BS to the building under consideration. Since these paths might have a varying range of azimuth angles, they will experience different levels of O2I

[2]Note that Fig. 15 shows only the mean angle and the strongest 5 paths for representation purposes; as can be observed from Fig. 12, the number of actual MPCs is much larger. The arrow lengths indicate the order of the magnitude but are not scaled according to the path gains.

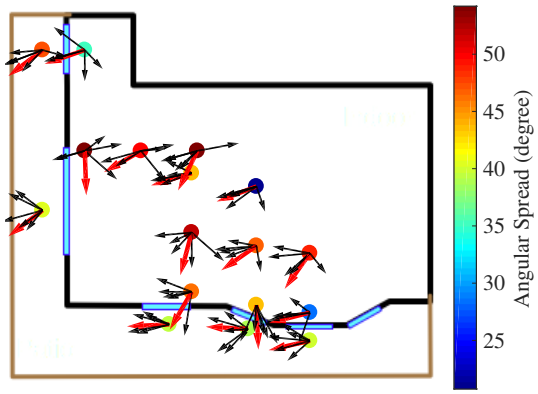

Fig. 15. Angular spreads for all RX locations in SFU1, red arrows indicate the mean direction of arrivals, black arrows indicate the RX beam directions for the five strongest MPCs.

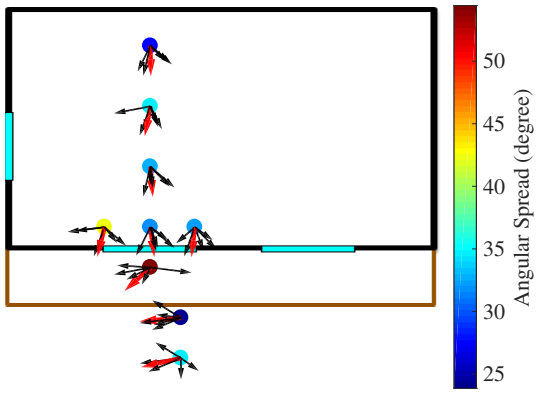

Fig. 16. Angular spreads for all RX locations in SFU2 for TX2, red arrows indicate the mean direction of arrivals, black arrows indicate the RX beam directions for the five strongest MPCs.

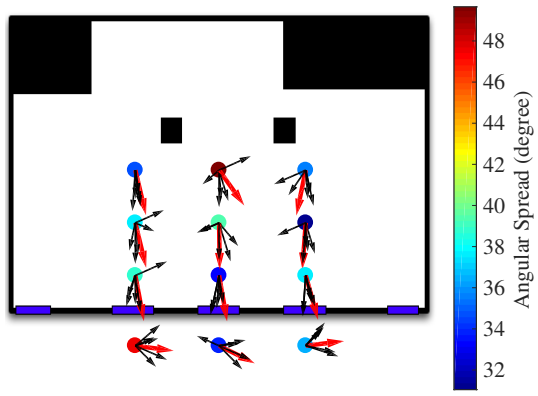

Fig. 17. Angular spreads for all RX locations in BOB, red arrows indicate the mean direction of arrivals, black arrows indicate the RX beam directions for the five strongest MPCs.

attenuation depending on their incident angles. Hence the O2I penetration will filter out some of the MPCs and favour others. The distribution of the angles incident on the building depends on the outside environment, while the filtering is a function of the building material and window layout. Consequently, observed propagation channel statistics and their differences for outdoor and indoor location will depend on site-specific details. Thus, it is crucial to design measurement campaigns that can consider the composite effect of these variables. It also becomes clear that a model that simply attenuates all MPCs by a "bulk" attenuation is not reflecting physical reality.

B. O2I Penetration Loss

In this section, we discuss O2I penetration loss for omni-directional and directional RX antennas. The omnidirectional path loss is calculated by combining all the TX-RX beams, while the directional RX simply chooses the best available beam in terms of RX power. As discussed above, this path loss is meaningful when assessing coverage, but should not be interpreted as constant loss for each MPC. Figs. 18, 19, 20 and 21 show the path loss for all RX points in all measurement locations. The points are ordered according to their distance from the windows (i.e., the outdoor points on the left are further away from the window and indoor points on the right are further away from the windows).

In the case of SFU1, the free space path loss for 185 m TX-RX distance at 28 GHz is 106.7 dB. However, due to shadowing from foliage, the path loss for the outdoor RX locations varies between 117 dB to 135 dB with a mean of 127.8 dB. According to the path loss model in [31], based on measurements in a similar environment, the anticipated path loss is 127.4 dB for the distance of 185 m which shows a good agreement with our results. In the case of SFU2, the two outdoor RX locations; *SFU2-O2* and *SFU2-O3* have almost line-of-sight LOS channels, hence the observed path loss values are similar to the LOS path loss for both TX1 and TX2. However, *O1*'s view to the TX is blocked by the neighboring structure and foliage resulting in a relatively higher path loss. Especially in the case of TX2, *SFU2-O1* has 13 dB higher path loss than other outdoor points, although they all have similar TX-RX distances. Due to foliage attenuation, the outdoor path loss values observed in the BOB vary from 111 dB to 122 dB with a mean of 117 dB, which indicates a loss due to foliage around 15 dB. Further investigations into foliage effects on path loss and delay spread at 28 GHz can be found in [32].

We first consider the impact of building material on the penetration loss by comparing points directly outside of the house and directly inside for three different scenarios SFU1, SFU2-TX2, and BOB that have similar incident angles. For SFU1 and SFU2-TX2 the excess losses are 10.0 dB and 8.1 dB, respectively. Care must be taken in the interpretation of the penetration loss in SFU2, in particular when using location O1 as a reference. The patio structure obstructs the propagation of quasi-line-of sight components, so that the outdoor attenuation is higher. Thus, outdoor locations SFU2-O2 and SFU2-O3 provide better estimates of the overall outdoor arriving power. If we take the other outdoor points

into account as well, the excess loss for SFU2-TX2 is as high as 16.6 dB, which is significantly higher than SFU1; this is due to the fact that only one facade has windows, as discussed in III-A. It is noteworthy that the BOB structure has a considerably higher pathloss than the SFU locations, namely more than 22 dB. As discussed earlier, in this location, the only viable paths from TX to RX are through the windows, which decreases the indoor RX power significantly, see Fig. 8 and Section III-A.

As seen in Figs. 18, 19, 20 and 21, we did not observe any significant increase in the path loss at the RX locations far away from the windows. Except at SFU1 (where the existence of the side windows leads to significant variations of the path loss within the room), all other measurements observed standard deviations of path loss within the room of only 1-2 dB without a significant dependency on the distance from the window. For BOB and SFU2, in parallel to the discussions in Section III-A, we see that for the indoor locations the MPCs with the highest power are either reflections from the window frames or the MPCs that are reflected/diffracted from outdoor objects near the RX and propagate almost perpendicularly into the building. Neither of these two propagation paths are significantly affected by the additional distance for the RX points deeper in the rooms.

The means and standard deviations of path loss values for all indoor and outdoor RX points are summarized in Table II. To investigate the mean O2I penetration loss, we subtract the mean outdoor path loss from indoor path loss values.[3] The corresponding means and standard deviations are given in Table II as well.

We first discuss the O2I penetration loss for omnidirectional RX. In case of SFU1, the O2I penetration loss has a mean of 10.6 dB and a standard deviation of 5.2 dB. Even though the two buildings are similar in terms of construction, the penetration loss for SFU2 is higher than SFU1. In SFU2, the mean penetration losses are 14.4 dB and 18.2 dB for TX1 and TX2, respectively. In case of SFU2-TX2 which has a similar incident angle with SFU1, the penetration loss is 8 dB higher than SFU1. As described in Section III-A, a likely cause is that the SFU1 is a corner house and has less blockage from the surrounding buildings. Furthermore, the standard deviations of the penetration losses are lower than SFU1, namely 1.8 dB and 2.3 dB for TX1 and TX2, respectively. When we compare TX1 and TX2 results for SFU2, we also see that the penetration loss is 4 dB higher for TX2, as the more grazing angle of incidence presents a more challenging situation for radio-waves' penetration. Similar to SFU2 for all BOB indoor locations, MPCs undergo similar propagation paths, the observed path losses do not vary significantly. The mean path losses for outdoor and indoor locations are 117 dB and 139.7 dB, respectively. Hence the mean excess loss due to O2I penetration is 22.7 dB and the standard deviation is 1.2 dB.

For indoor RX points in SFUs the directional path loss is approximately 2.5 dB higher than the omnidirectional path loss. However, the differences between directional and omnidirectional path losses for outdoor RX points are around 1 dB. Consequently, the directional path loss is approximately 1.5 dB more than the omnidirectional case for all SFU measurements. The difference is more prominent in the case of BOB and the directional penetration losses are 2.5 dB more than the omnidirectional case. Note that this excludes the antenna gain, which needs to be considered for a realistic link budget.

[3]Note the observed distribution is affected by both the varying O2I penetration losses and the indoor propagation channel.

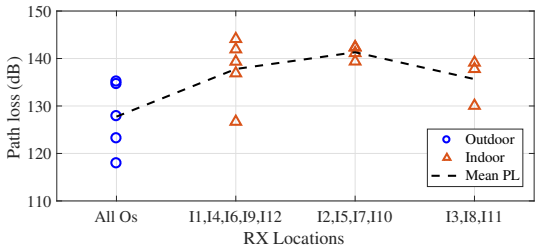

Fig. 18. Omnidirectional path loss vs the RX locations in SFU1, the indoor locations ordered according to the distance from the window, the RX locations with the same distance from the windows are grouped together.

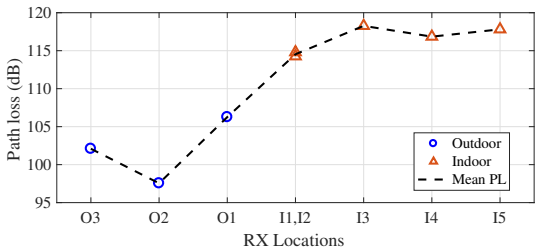

Fig. 19. Omnidirectional path loss vs the RX locations in SFU2-TX1, the indoor locations ordered according to the distance from the window, the RX locations with the same distance from the windows are grouped together.

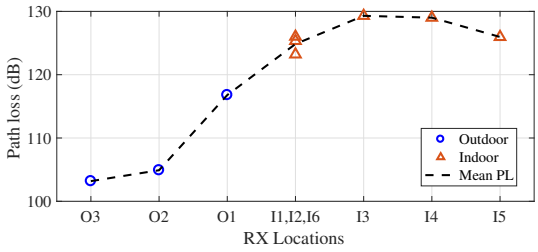

Fig. 20. Omnidirectional path loss vs the RX locations in SFU2-TX2 the indoor locations ordered according to the distance from the window, the RX locations with the same distance from the windows are grouped together.

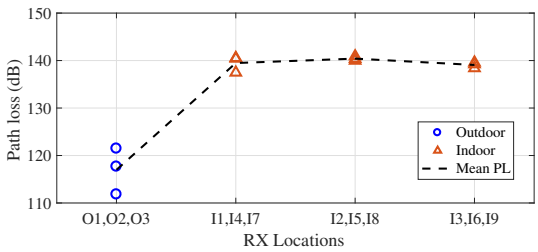

Fig. 21. Omnidirectional path loss vs the RX locations in BOB, the indoor locations ordered according to the distance from the window, the RX locations with the same distance from the windows are grouped together.

TABLE II
MEAN PATH LOSS AND PENETRATION LOSS VALUES

	Location	Outdoor		Indoor		Penetration Loss	
		μ	σ	μ	σ	μ	σ
omnidirectional	SFU1	127.8 dB	7.4 dB	138.4 dB	5.2 dB	10.6 dB	5.2 dB
	SFU2 - TX1	102.0 dB	4.4 dB	116.4 dB	1.8 dB	14.4 dB	1.8 dB
	SFU2 - TX2	108.3 dB	7.4 dB	126.5 dB	2.3 dB	18.2 dB	2.3 dB
	BOB	117.0 dB	4.9 dB	139.7 dB	1.2 dB	22.7 dB	1.2 dB
directional	SFU1	128.6 dB	6.4 dB	140.9 dB	7.5 dB	12.3 dB	7.5 dB
	SFU2 - TX1	102.8 dB	5.5 dB	119.0 dB	1.8 dB	16.1 dB	1.8 dB
	SFU2 - TX2	109.9 dB	9.7 dB	128.8 dB	3.0 dB	19.0 dB	3.0 dB
	BOB	117.9 dB	5.6 dB	143.1 dB	1.3 dB	25.2 dB	1.3 dB

C. Root Mean Square Delay Spread

Similar to the penetration loss, we investigate the RMS-DS for the cases where the RX has an omnidirectional view or if it selects the RX beam with the highest power (i.e., the directional RX).

Fig. 22 shows a comparison between outdoor and indoor PDPs from SFU2-TX2. In this case, the outdoor and indoor RMS-DS are 35 ns and 75 ns RMS-DS, respectively. Although the indoor environments adds additional MPCs due to reflections from the surrounding walls and furniture, relative delays of these MPCs are not high enough to affect the RMS-DS significantly. Rather, in the scenarios investigated in the paper, although the O2I propagation does not introduce new MPCs with large excess delays, the varying amount of penetration loss affecting MPCs causes significant changes in RMS-DS. In line with the discussion of Section III-A, we see that early MPCs, which have grazing incidence, have stronger attenuation than later arriving components; this explains the increase in the delay spread. In addition, we observed that the variation of the indoor RMS-DS values is not significantly higher or lower compared to the outdoor reference points. This indicates that the variation is not caused by indoor reflections, but it is actually caused by the different subset of MPCs (with large excess delay and varying incident angles) arriving to the different RX locations.

Following our earlier discussions in Section III-A, O2I penetration forces all paths into a relatively limited angular range. Especially, in BOB and SFU2 this process is more prominent, and results in directional RMS-DS values similar to the omnidirectional ones for indoor locations even though the outdoor directional RMS-DS values are significantly less than the omnidirectional ones for these locations.

The mean and the median RMS-DS values are listed in Table III. As the RMS-DS is generally modelled with a Log-normal distribution, we provide the corresponding mean and standard deviation for each measurement environment for readers' reference. If we compare our findings with the O2I channel model parameters suggested in Table 7.5-6 in the most recent 3GPP standard for mm-wave frequency channels [33]. In terms of base-station height and the environment type, the urban micro (UMi) scenario presented in the report is the closest one to our measurements. However, the UMi channel model parameters are only given for a street canyon scenario. As discussed in Section III-A, the relative locations of the surrounding buildings not only have an effect on the absolute values of the channel parameters, but they also affect how the channel parameters change during the O2I penetration. For 28 GHz UMi, the 3GPP standard reports the means of the logarithm of the RMS-DS μ_{DS} as -7.49 for LOS, -7.18 for NLOS and -6.62 for O2I. Since these values are given for a street canyon scenario, as one would expect that they are significantly higher than our observations. Especially in the

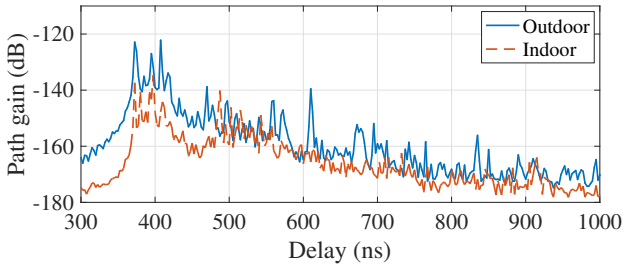

Fig. 22. Sample omnidirectional PDPs for outdoor and indoor RX location for SFU2

TABLE III
RMS-DS STATISTICS

	Location	Mean (ns)	Median (ns)	Logarithmic Scale	
				μ	σ
omnidirectional	SFU1-Indoor	26.15	27.36	-7.61	0.19
	SFU1-Outdoor	23.89	23.32	-7.66	0.23
	SFU2-Indoor	36.74	25.73	-7.51	0.28
	SFU2-Outdoor	18.26	14.18	-7.79	0.24
	BOB-Indoor	51.99	47.86	-7.32	0.06
	BOB-Outdoor	37.88	28.01	-7.46	0.22
directional	SFU1-Indoor	18.09	16.11	-7.79	0.21
	SFU1-Outdoor	9.66	12.37	-8.09	0.33
	SFU2-Indoor	26.80	17.64	-7.70	0.38
	SFU2-Outdoor	7.55	6.51	-8.19	0.29
	BOB-Indoor	46.18	43.18	-7.41	0.34
	BOB-Outdoor	14.37	14.26	-7.84	0.05

O2I case the prescribed μ_{DS} corresponds to $240\,\text{ns}$ which is almost an order of magnitude larger than our measurements. Furthermore the difference between outdoor and indoor RMS-DS is much higher than our observation. Consequently, these values are not applicable to the residential small cell environments. From our observations, for a given house location, if the $\mu_{\text{DS,out}}$ of the outdoor RMS-DS is known, the indoor can be estimated by $\mu_{\text{DS,in}} = \mu_{\text{DS,out}} + 0.2$ for an omnidirectional RX, and by $\mu_{\text{DS,in}} = \mu_{\text{DS,out}} + 0.45$ for a directional RX, when the building under study has a single illuminated wall. If the structure and environment allow MPCs to penetrate into the building from more than one side, then the indoor RMS-DS only increases slightly i.e., $\mu_{\text{DS,in}} = \mu_{\text{DS,out}} + 0.05$ for the omnidirectional RX and $\mu_{\text{DS,in}} = \mu_{\text{DS,out}} + 0.3$ for directional RX.

D. Angular Spread

In this section, we study the DoA angular spread of the MPCs shown in Section III-A and Figs. 15, 16 and 17. In parallel to our earlier observations, for the indoor RX points SFU1, the observed subset of paths varies depends on the exact location within the house. Consequently, the angular spread values vary from 21° to 55° although all outdoor points have angular spreads in the range of 38.5° to 47°. This variation within the room has important implications for system design. Deployment of antennas indoors might require higher adaptivity of the antenna pattern, and the angular spread could change drastically when relocating the antenna within a room. The wide range of mean angle of arrivals shown in Fig. 15 supports this observation as well. Additionally, the mean angular spread for indoor is 43.5°, which is quite similar to the outdoor angular spread of 41°.

For both SFU2 and BOB, the main path of propagation is via the front side of the house, due to blockage by the neighboring structure for SFU2 and lack of side windows for BOB. Table IV summarizes the statistics of the angular spreads for all SFU and BOB angular spread values. Angular spread is commonly modelled with a Log-normal distribution. Although the number of measurement points is limited for some cases, we provide means and standard deviations of the (logarithmic) angular spreads of the measured data in Table IV as well. The observed mean angular spreads are slightly smaller for the indoor compared to the outdoor RX points for both cases, see Table IV. However, in the case of BOB, due to the limited number of outdoor locations, it is not certain that the results can be generalized. Furthermore, the observed means and deviations for indoor are quite similar for these two structures even though they are built with significantly different types of materials. This indicates that the effects of the floor plan (i.e., number and dimensions of windows) are prominent compared to the effects of the building material.

Similar to the RMS-DS, we compare our findings with the O2I channel model parameters suggested for the UMi scenario in Table 7.5-6 in [33]. The 3GPP standard also reports the mean of the logarithms of the angular spread of azimuth DoA for LOS, NLOS, and O2I as 1.61, 1.69 and 1.76, respectively. In linear scale the angular spreads for LOS and NLOS are 40.7° and 49°, respectively. In addition, the O2I angular spread specified is 57.5°, which is significantly higher than our observation. Furthermore, the average indoor angular spreads are approximately 20% and 40% higher than the outdoor NLOS and LOS points. We observed this increase in only around 5% for the SFU cases. Furthermore, in case of BOB, which is a brick building (i.e., penetration is only possible via windows), the mean indoor angular spread was 5% smaller than the outdoor values.

TABLE IV
ANGULAR SPREAD STATISTICS

Location	Mean	Median	Logarithmic Scale	
			μ	σ
SFU1-Indoor	43.51°	46.31°	1.62	0.13
SFU1-Outdoor	41.00°	39.77°	1.61	0.04
SFU2-Indoor	36.46°	34.49°	1.56	0.07
SFU2-Outdoor	38.12°	37.25°	1.54	0.18
BOB-Indoor	37.53°	37.60°	1.57	0.06
BOB-Outdoor	39.21°	36.32°	1.59	0.07

E. Receiver Angular Diversity

We next analyze the available beam diversity in the various measured environments. This is important in case that the strongest MPC is blocked, e.g., by a human person walking through the propagation path. We define the available diversity as follows: we divide the 360° azimuth into 8 sectors (of 45° each - we assume that a human can block one such sector - an assumption that of course depends on the distance between the human and the RX). The RX sector centers are chosen as [0°, 45°, 90°,..., 315°] and all BS sectors are active. The RX power for each sector is calculated by adding up all detected MPCs within the same sector. We then determine the sector with the highest RX power and the number of other sectors in which the arriving power is within 10 dB of the best sector. We name these sectors as selectable sectors and note the number of selectable sectors as N_s. This measure thus indicates whether switching to a different direction can maintain the connection. We also quantify the RX power difference between the best and second best sectors as Δ_p.

Figs. 23, 24, 25 and 26 show the relative received power in each sector (in descending order) with respect to the best sector for that RX location for all measurement environments. The dashed line indicates where the received power drops 10 dB below the best sector, so the number of sectors below the dashed line indicates the number of selectable sectors (i.e., N_s) for a given RX location[4].

In line with the large range of angular spread values for the SFU1 indoor RX locations, the N_s also varies from 1 to 6 with a mean of 3.9, see Fig. 23. The Δ_p's are 4 dB and 3.2 dB for indoor and outdoor, respectively. In case of SFU2 for both TX1 and TX2, *SFU2-O1*, which is the point right outside of the window, suffers from foliage and neighboring

[4]The 10 dB threshold is chosen arbitrarily, similar investigations can be performed for other threshold levels by investigating Figs. 23, 24, 25 and 26.

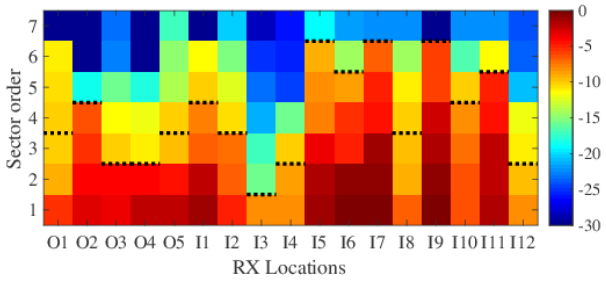

Fig. 23. SFU1 - Ordered relative power (dB) of other sectors with respect to the sector with the highest power, dashed line indicated where it drops below 10 dB

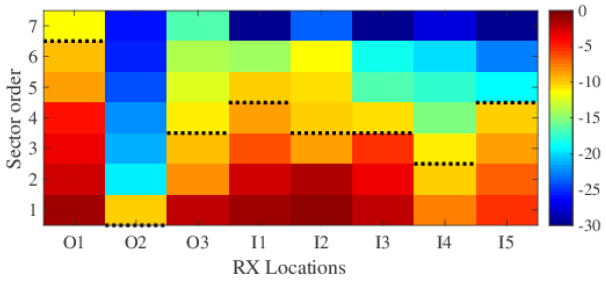

Fig. 24. SFU2 TX1 - Ordered relative power (dB) of other sectors with respect to the sector with the highest power, dashed line indicated where it drops below 10 dB

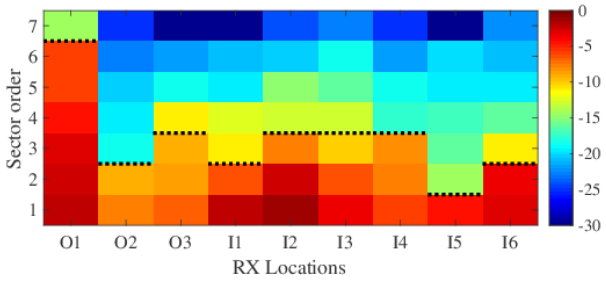

Fig. 25. SFU2 TX2 - Ordered relative power (dB) of other sectors with respect to the sector with the highest power, dashed line indicated where it drops below 10 dB

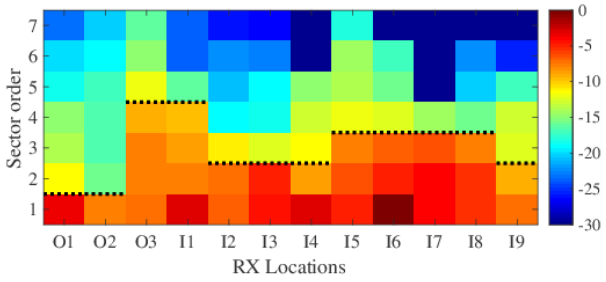

Fig. 26. BOB - Ordered relative power (dB) of other sectors with respect to the sector with the highest power, dashed line indicated where it drops below 10 dB

structure. Consequently at this point, there are several indirect paths with varying DoAs. In addition, the RX also receives several reflections from the house itself, consequently, unlike other outdoor RX locations, 6 out of 8 sectors are within 10 dB of the best sector for both TX locations, as seen in Figs. 24 and 25. At the other two outdoor RX locations, the N_s's are 0 to 3. In case of indoors, the mean N_s's are 3.2 and 2.3 for TX1 and TX2, respectively. Furthermore, the expected loss in the received power when the best sector is blocked (i.e., Δ_p) are 5.1 dB for outdoor and 3.5 dB for indoor. Another interesting observation is that the second-best sector is a neighboring sector to the best one for 10 out of 11 indoor RX locations for the SFU2, while this ratio is only 6 out of 12 for the SFU1. Hence the availability of a side window affects the correlation of the received power for neighboring sectors.

In case of BOB, the mean N_s's are 2.7 and all indoor RX locations have a N_s between 2 to 4. The mean Δ_p's are 6.3 dB for outdoor and 4.3 dB for indoor which is slightly higher than in the other measurement locations. Similar to SFU2, for most of the cases (7 out of 9), the second best sector is a neighboring sector of the best one. This is anticipated as both structures only allow MPCs from a limited azimuth range.

Table V compares N_s and Δ_p values for 45° sectors with ones for 30° and 60° sectors. For all environments, the mean Δ_p is almost always smaller for indoor RXs compared to the outdoor RXs. In summary, we observed that for most the indoor locations, there is at least one more sector within 10 dB of the main sector, regardless of the sector width. Additionally, the mean RX power difference between the best and the second-best section varies from 3 to 5 dB. Considering the excess losses due to body blockage at 28 GHz are shown to be as high as 15 dB [34], [35], it is clearly beneficial to employ a structure with adaptive beam-forming for the indoor environments.

IV. Conclusions

In this paper, we presented measurements at 28 GHz investigating effects of outdoor to indoor penetration. The measurements performed in a challenging scenario where the direct path from the TX has a quasi-grazing angle to the building under investigation. We observed that the O2I penetration losses vary from 10 dB to 18 dB for a single family unit depending on the site-specific details such as place of the house on the street or the incident angle from the base station to the house. In the case of a brick building, the penetration loss is as high as 23 dB. Furthermore, the penetration loss is 2-3 dB higher when the RX is forced to choose a single directional beam with 12° half power beam width for all cases. For buildings with a single visible front from the TX that would allow O2I penetration, we have not observed any significant change in the indoor RX power with on the indoor location or the distance from the window. However, the RX power fluctuates more than 10 dB in the presence of a second side offering an alternative path of propagation. Perhaps most importantly, we find that the common approach of adding a "bulk" penetration loss to an outdoor model is not a viable way to model outdoor-to-indoor mm-wave channels. Neither is a

TABLE V
DIVERSITY STATISTICS, N_s IS THE NUMBER OF SELECTABLE SECTORS AND Δ IS THE

Location	30° Sector		45° Sector		60° Sector	
	N_s out of 11	Δ (dB)	N_s out of 7	Δ(dB)	N_s out of 5	Δ (dB)
SFU1-Indoor	5.08	4.45	3.9	3.2	3.25	3.89
SFU1-Outdoor	3.80	3.59	2.8	4	2.4	3.63
SFU2-TX1-Indoor	4	2.94	3.2	3.47	2.2	3.16
SFU2-TX1-Outdoor	4.67	3.78	3	4.48	2.67	4.74
SFU2-TX2-Indoor	3.5	1.43	2.33	3.38	2.2	1.80
SFU2-TX2-Outdoor	4.33	5.42	3.67	5.64	2.67	5.10
BOB-Indoor	3.78	2.63	2.7	4.3	2	2.33
BOB-Outdoor	2.33	6.35	2	6.3	2	6.09

concatenation of an outdoor channel with an indoor channel; rather the environment-specific interaction has to be accounted for. Thus, effects of O2I propagation on the DoA and delay spread statistics are more affected by the floor plan and the relative location of the building under investigation with respect to the surrounding structures rather than its building materials.

Further investigations into the available beam-diversity showed that an adaptive beam-forming could improve the mean RX SNR by 5 to 7 dB in case the best sector is blocked by a human body. Finally, we compare our findings about RMS-DS and angular spread with the most recent 3GPP standard and find that the type of environment we measured in is not represented by an existing model; we therefore provided model parameters for a "suburban O2I" environment, which will be important for 5G deployment.

REFERENCES

[1] C. U. Bas, R. Wang, T. Choi, S. Hur, K. Whang, J. Park, J. Zhang, and A. F. Molisch, "Outdoor to indoor penetration loss at 28 GHz for fixed wireless access," in *2018 IEEE International Conference on Communications (ICC)*, May 2018, pp. 1–6.

[2] C. V. Forecast, "Cisco visual networking index: Global mobile data traffic forecast update, 2016–2021 white paper," *Cisco Public Information*, March 2017.

[3] J. G. Andrews, S. Buzzi, W. Choi, S. V. Hanly, A. Lozano, A. C. Soong, and J. C. Zhang, "What will 5G be?" *Selected Areas in Communications, IEEE Journal on*, vol. 32, no. 6, pp. 1065–1082, June 2014.

[4] F. Boccardi, R. W. Heath, A. Lozano, T. L. Marzetta, and P. Popovski, "Five disruptive technology directions for 5G," *IEEE Communications Magazine*, vol. 52, no. 2, pp. 74–80, February 2014.

[5] N. Al-Falahy and O. Y. Alani, "Technologies for 5G networks: Challenges and opportunities," *IT Professional*, vol. 19, no. 1, pp. 12–20, January 2017.

[6] Z. Pi, J. Choi, and R. Heath, "Millimeter-wave gigabit broadband evolution toward 5g: fixed access and backhaul," *IEEE Communications Magazine*, vol. 54, no. 4, pp. 138–144, April 2016.

[7] J. Wells, "Faster than fiber: The future of multi-G/s wireless," *IEEE microwave magazine*, vol. 10, no. 3, May 2009.

[8] P. B. Papazian, G. A. Hufford, R. J. Achatz, and R. Hoffman, "Study of the local multipoint distribution service radio channel," *IEEE Transactions on Broadcasting*, vol. 43, no. 2, pp. 175–184, June 1997.

[9] T. Rappaport, S. Sun, R. Mayzus, H. Zhao, Y. Azar, K. Wang, G. N. Wong, J. K. Schulz, M. Samimi, and F. Gutierrez, "Millimeter wave mobile communications for 5G cellular: It will work!" *Access, IEEE*, vol. 1, pp. 335–349, May 2013.

[10] W. Roh, J. Y. Seol, J. Park, B. Lee, J. Lee, Y. Kim, J. Cho, K. Cheun, and F. Aryanfar, "Millimeter-wave beamforming as an enabling technology for 5G cellular communications: theoretical feasibility and prototype results," *IEEE Communications Magazine*, vol. 52, no. 2, pp. 106–113, February 2014.

[11] A. F. Molisch, A. Karttunen, R. Wang, C. U. Bas, S. Hur, J. Park, and J. Zhang, "Millimeter-wave channels in urban environments," in *2016 10th European Conference on Antennas and Propagation (EuCAP)*, April 2016, pp. 1–5.

[12] S. Hur, Y.-J. Cho, T. Kim, J. Park, A. Molisch, K. Haneda, and M. Peter, "Wideband spatial channel model in an urban cellular environments at 28 GHz," in *Antennas and Propagation (EuCAP), 2015 9th European Conference on*, April 2015, pp. 1–5.

[13] M.-D. Kim, J. Liang, Y. K. Yoon, and J. H. Kim, "28 GHz path loss measurements in urban environments using wideband channel sounder," in *Antennas and Propagation USNC/URSI National Radio Science Meeting, 2015 IEEE International Symposium on*, July 2015, pp. 1798–1799.

[14] S. Hur, Y. J. Cho, J. Lee, N.-G. Kang, J. Park, and H. Benn, "Synchronous channel sounder using horn antenna and indoor measurements on 28 GHz," in *2014 IEEE International Black Sea Conference on Communications and Networking (BlackSeaCom)*, May 2014, pp. 83–87.

[15] C. U. Bas, R. Wang, S. Sangodoyin, S. Hur, K. Whang, J. Park, J. Zhang, and A. F. Molisch, "Dynamic double directional propagation channel measurements at 28 GHz - Invited paper," in *2018 IEEE 87th Vehicular Technology Conference (VTC Spring)*, June 2018, pp. 1–6.

[16] K. Haneda, J. Järveläinen, A. Karttunen, M. Kyrö, and J. Putkonen, "A statistical spatio-temporal radio channel model for large indoor environments at 60 and 70 GHz," *EEE Transactions on Antennas and Propagation*, vol. 63, pp. 2694–2704, March 2015.

[17] J. Ko, K. Lee, Y. J. Cho, S. Oh, S. Hur, N. G. Kang, J. Park, D. J. Park, and D. H. Cho, "Feasibility study and spatial-temporal characteristics analysis for 28 GHz outdoor wireless channel modelling," *IET Communications*, vol. 10, no. 17, pp. 2352–2362, November 2016.

[18] C. Larsson, F. Harrysson, B. E. Olsson, and J. E. Berg, "An outdoor-to-indoor propagation scenario at 28 GHz," in *The 8th European Conference on Antennas and Propagation (EuCAP 2014)*, April 2014, pp. 3301–3304.

[19] J. Du, D. Chizhik, R. Feick, G. Castro, M. Rodrguez, and R. A. Valenzuela, "Suburban Residential Building Penetration Loss at 28 GHz for Fixed Wireless Access," *IEEE Wireless Communications Letters*, pp. 1–1, May 2018.

[20] I. Rodriguez, H. C. Nguyen, I. Z. Kovcs, T. B. Srensen, and P. Mogensen, "An empirical outdoor-to-indoor path loss model from below 6 GHz to cm-Wave frequency bands," *IEEE Antennas and Wireless Propagation Letters*, vol. 16, pp. 1329–1332, December 2017.

[21] H. Zhao, R. Mayzus, S. Sun, M. Samimi, J. K. Schulz, Y. Azar, K. Wang, G. N. Wong, F. Gutierrez, and T. S. Rappaport, "28 GHz millimeter wave cellular communication measurements for reflection and penetration loss in and around buildings in New York city," in *2013 IEEE International Conference on Communications (ICC)*, June 2013, pp. 5163–5167.

[22] K. Haneda, J. Zhang, L. Tan, G. Liu, Y. Zheng, H. Asplund, J. Li, Y. Wang, D. Steer, C. Li *et al.*, "5G 3GPP-like channel models for outdoor urban microcellular and macrocellular environments," in *Vehicular Technology Conference (VTC Spring), 2016 IEEE 83rd*. IEEE, July 2016, pp. 1–7.

[23] N. Tran, T. Imai, and Y. Okumura, "Outdoor-to-indoor channel characteristics at 20 GHz," in *2016 International Symposium on Antennas and Propagation (ISAP)*, October 2016, pp. 612–613.

[24] T. Imai, K. Kitao, N. Tran, N. Omaki, Y. Okumura, and K. Nishimori, "Outdoor-to-Indoor path loss modeling for 0.8 to 37 GHz band," in *2016*

10th European Conference on Antennas and Propagation (EuCAP), April 2016, pp. 1–4.

[25] C. A. L. Diakhate, J. M. Conrat, J. C. Cousin, and A. Sibille, "Millimeter-wave outdoor-to-indoor channel measurements at 3, 10, 17 and 60 GHz," in *2017 11th European Conference on Antennas and Propagation (EUCAP)*, March 2017, pp. 1798–1802.

[26] C. U. Bas, R. Wang, D. Psychoudakis, T. Henige, R. Monroe, J. Park, J. Zhang, and A. F. Molisch, "A real-time millimeter-wave phased array MIMO channel sounder," in *2017 IEEE 86th Vehicular Technology Conference (VTC-Fall)*, September 2017, pp. 1–6.

[27] C. U. Bas, R. Wang, S. Sangodoyin, D. Psychoudakis, T. Henige, R. Monroe, J. Park, J. Zhang, and A. F. Molisch, "Real-time millimeter-wave MIMO channel sounder for dynamic directional measurements," submitted.

[28] M. Friese, "Multitone signals with low crest factor," *IEEE Transactions on Communications*, vol. 45, no. 10, pp. 1338–1344, Oct 1997.

[29] A. F. Molisch, *Wireless communications*, 2nd ed. IEEE Press - Wiley, 2010.

[30] B. H. Fleury, "First- and second-order characterization of direction dispersion and space selectivity in the radio channel," *IEEE Transactions on Information Theory*, vol. 46, no. 6, pp. 2027–2044, September 2000.

[31] C. U. Bas, R. Wang, S. Sangodoyin, S. Hur, K. Whang, J. Park, J. Zhang, and A. F. Molisch, "28 GHz microcell measurement campaign for residential environment," in *GLOBECOM 2017 - 2017 IEEE Global Communications Conference*, December 2017, pp. 1–6.

[32] ——, "28 GHz foliage propagation channel measurements," in *GLOBECOM 2018 - 2018 IEEE Global Communications Conference*, December 2018.

[33] 3GPP, "5G; Study on channel model for frequencies from 0.5 to 100 GHz," *3GPP TR 38.901 version 14.3.0 Release 14*, January 2018.

[34] X. Chen, L. Tian, P. Tang, and J. Zhang, "Modelling of Human Body Shadowing Based on 28 GHz Indoor Measurement Results," in *2016 IEEE 84th Vehicular Technology Conference (VTC-Fall)*, September 2016, pp. 1–5.

[35] T. Choi, C. U. Bas, R. Wang, S. Sangodoyin, S. Hur, J. Park, J. Zhang, and A. F. Molisch, "Measurement based modelling of human body shadowing at 28 GHz," in *GLOBECOM 2018 - 2018 IEEE Global Communications Conference*, December 2018.